

# Process planning based on cylindrical or conical surfaces for five-axis wire and arc additive manufacturing

*Fusheng Dai*

School of Mechanical Science and Engineering, Huazhong University of Science and Technology, Wuhan, China

*Haïou Zhang*

State Key Laboratory of Digital Manufacturing Equipment and Technology,  
Huazhong University of Science and Technology, Wuhan, China, and

*Runsheng Li*

School of Mechanical Science and Engineering, Huazhong University of Science and Technology, Wuhan, China

## Abstract

**Purpose** – The study aims to fabricate large metal components with overhangs built on cylindrical or conical surfaces with a high dimensional precision. It proposes methods to address the problems of generating tool-paths on cylindrical or conical surfaces simply and precisely, and planning the welding process on these developable surfaces.

**Design/methodology/approach** – The paper presents the algorithm of tool-paths planning on conical surfaces using a parametric slicing equation and a spatial mapping method and deduces the algorithm of five-axis transformation by addressing the rotating question of two sequential points. The welding process is investigated with a regression fitting model on a flat surface, and experimented on a conical surface, which can be flattened onto a flat surface.

**Findings** – The paper provides slicing and path-mapping expressions for cylindrical and conical surfaces and a curvature-speed-width (CSW) model for wire and arc additive manufacturing to improve the surface appearances. The path-planning method and CSW model can be applied in the five-axis fabrication of the prototype of an underwater thruster. The CSW model has a confidence coefficient of 98.02% and root mean squared error of 0.2777 mm. The reverse measuring of the finished blades shows the residual deformation: an average positive deformation of about 0.5546 mm on one side of the blades and an average negative deformation of about  $-0.4718$  mm on the other side.

**Research limitations/implications** – Because of the chosen research approach, the research results may lack generalizability for the fabrication based on arbitrary surfaces.

**Originality/value** – This paper presented an integrated slicing, tool-path planning and welding process planning method for five-axis wire and arc additive manufacturing.

**Keywords** Additive manufacturing, Process planning, Path planning, Arc welding, Five-axis, Overhangs, Tool-path planning

**Paper type** Research paper

## 1. Introduction

Additive manufacturing (AM) is a technique based on the dispersion-deposition principle, which takes layer by layer overlapping manner to have a “bottom-up” freeform fabrication from computer aided design (CAD) model data. It is a different form and has many advantages over traditional manufacturing processes such as time effective, cost effective and market responsive (Youheng *et al.*, 2017). The “dispersion” of AM is commonly carried out by Computer-Aided Path Planning, which consists of dispersing 3D CAD model into a set of slices and generating filling paths on these slices.

A technique of AM of the entire component from the deposition of weld metal has been in practice since 1920 which is now being exercised as a wire arc additive manufacturing (WAAM) technique (Derekar, 2018). WAAM is an additive manufacturing technology that uses wire feedstock to produce parts by depositing material layer by layer onto a substrate plate, using welding technology controlled by a robot or computer numerical control (CNC) machine (Derekar, 2018). Compared with laser engineered net shaping, selective laser sintering and electron beam melting, WAAM has unique efficiency and cost advantages especially in the deposition of large thick-walled parts (Youheng *et al.*, 2017). The part may be machined to its final dimensions either during deposition or after deposition is complete, depending on the application (Williams *et al.*, 2016; Lockett *et al.*, 2017).

The current issue and full text archive of this journal is available on Emerald Insight at: <https://www.emerald.com/insight/1355-2546.htm>



Rapid Prototyping Journal  
26/8 (2020) 1405–1420  
© Emerald Publishing Limited [ISSN 1355-2546]  
[DOI 10.1108/RPJ-01-2020-0001]

This work was supported by Special Research Program of Civil Aircraft (Grant no. MJZ-2017-G-\*\*) and Technology Innovation Special Project of Hubei Province (Grant no. 2017AAA003).

Received 2 January 2020

Revised 16 May 2020

Accepted 25 May 2020

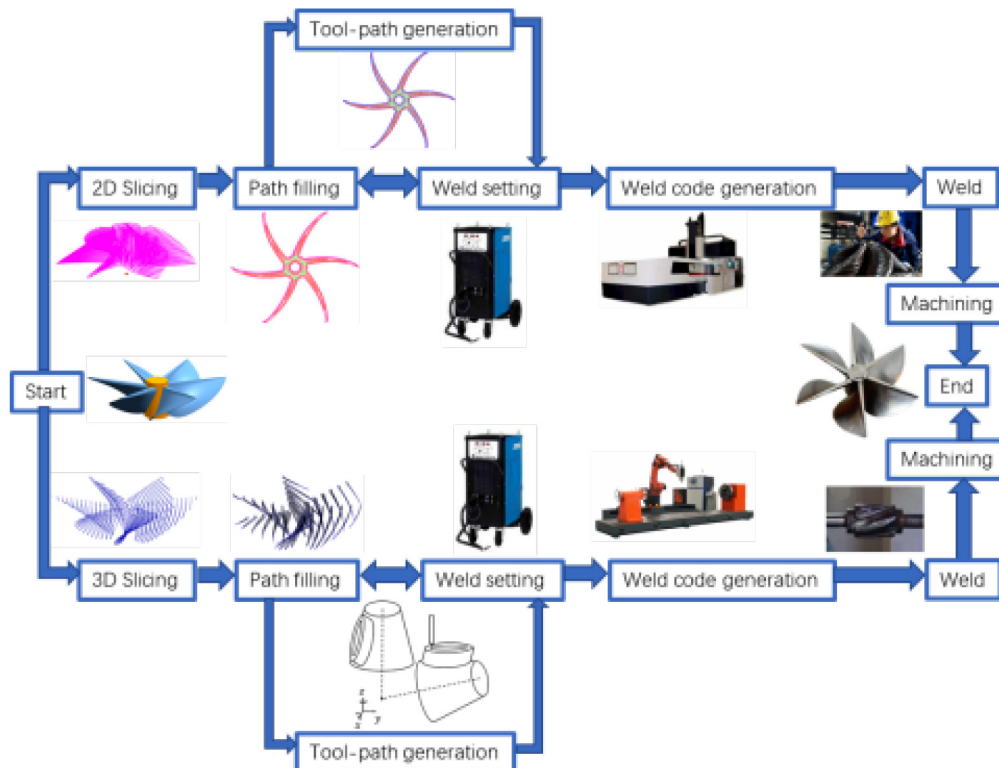
Generally, process planning for a WAAM system involves 3D modeling, slicing, path filling, tool-path generation, weld setting, weld code generation, weld and post-process machining, as shown in Figure 1. The 3D models are sliced into a set of contours, whether by a set of 2D planes or by a set of 3D surfaces. Through path planning algorithms, these contours are filled with parallel lines (Dunlavey, 1983; Rajan *et al.*, 2001; Park and Choi, 2000), parallel contours (Farouki *et al.*, 1995; Yang *et al.*, 2002), spiral lines (Li *et al.*, 1994; Wang *et al.*, 2001) or fractal paths (Yang *et al.*, 2003; Bertoldi *et al.*, 1998). The tool-paths are generated by adding the tooling information. The weld process is determined according to experiments. The weld parameter controls the path filling variables, such as the distance between two contiguous slices, and the distance between two contiguous filling paths; it also influences the path post-processing, like path fairing or transformation for multi-axes deposition. Subsequently, together with the selected weld parameters, the tool-paths are transferred into an integrated robot or CNC machine code file. Finally, a near net-shaped deposit is produced automatically by the arc welding system. Post-process machining is usually required to produce a finished component (Rajan *et al.*, 2001). There we can see two different process planning routes: One is carried out on flat surfaces, and the other gets all the deposition paths on 3D surfaces. Compared with the planer slicing method, the 3D slicing method fabricates a component according to its geodesic features. The part may be mounted on a part-rotator so that the build direction can be changed during deposition (Williams *et al.*, 2016).

In the past years, many researchers have worked for the process planning of WAAM. To acquire better deposition quality, molten pool stability, travel speed, wire speed and

proper process matching are proved to be crucial (Yanjiang and Ziqu, 2019; Xiong *et al.*, 2018; Xiong *et al.*, 2017; Zhou *et al.*, 2016). Besides, outer force from a micro roller can help to improve the geometrical accuracy of the built features (Xie *et al.*, 2015). These works focused on process planning based on planer slicing.

As the development of the multi-axis manufacturing system, path planning methods such as multi-direction adaptive slicing and curved printing have been widely studied. Singh and Dutta (2001) and Sundaram and Choi (2004) disintegrated an object into a manufacturable part and another part which is not manufacturable according to its overhang angles, but the slicing direction should be designated interactively by users. Zhang and Liou (2004) optimized the slicing direction using a Gaussian map to define a spherical crown; however, without considering the tangent estimation error of the tessellated model. In addition, Ruan *et al.* (2007), Kabakabala *et al.* (2010) and Ren *et al.* (2008) researched on variable slicing direction based on the centroid axis, but the precision of the centroid axis is strongly associated with the layer thickness. The geodesic information of the original model, such as normal and tangents vectors and surface feature information, are important for multi-axis AM. Surface feature information indicates new slicing approaches, such as cylindrical or conical slicing presented in this paper, generating contours on cylindrical or conical surfaces. In the literature, Wang *et al.* (2015) generated parallel contours on curved surface by mapping the surface onto a planar plane, but the surface would have distortions after mapping, making the distance between any two neighboring contours unequal. Chen and Tang (2019) reduced the stair-

Figure 1 Process planning for a WAAM system



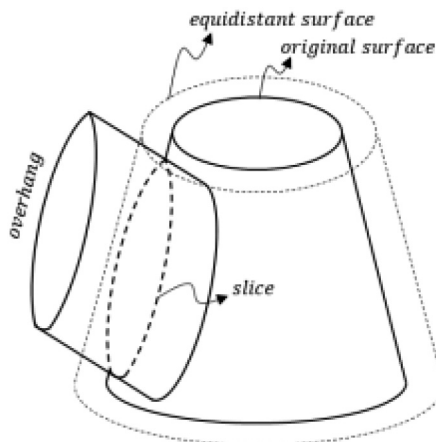
step effect by allowing the sliced layers to have variable thicknesses and adjusting the build direction adaptively with respect to the surface normal. Dai *et al.* (2018) and Xu *et al.* (2019) proposed volume printing methods to fabricate parts without support structures. Such volume printing can be used to fabricate complicated shaped parts, but makes it harder to fabricate parts with usable surface feature information, such as overhangs built on ruled surfaces. Ding *et al.* (2017, 2018) introduced a tool-path planning method for multi-axis laser-based metal deposition on revolved surfaces by a spatial mapping method in a cylindrical coordinate. However, the filling paths were not strictly equidistant if the revolved surfaces were not cylindrical surfaces.

To address the process planning problems above, we present an integrated slicing, tool-path planning and welding process planning method for five-axis additive processing modules. The structures built on a cylindrical or conical surface is commonly used in the industry. Such surfaces can be described with a unit equation, providing better conditions for the calculation of slicing and path filling. A set of equidistant cylindrical or conical surfaces are generated to slice the triangle-meshed 3D model. As cylindrical and conical surfaces are developable, these slices can be flattened onto planes without distortion, and be mapped to the surfaces after being filled with equidistant paths. The conventional path filling strategies are applicable when these slices are flattened onto planes. To realize the five-axis manufacturing, a five-axis algorithm is deduced, making it possible to adjust the orientation of the built piece dynamically. What is more, a curvature-speed-width (CSW) model is introduced to control the width of the bead by coupling the curve curvature with proper travel speed.

## 2. Path planning on cylindrical or conical surfaces

To fabricate an overhang built on a curved surface by AM, equidistant surfaces of the original surface are generated to slice the overhang (Figure 2). The cylindrical or conical surfaces can be described with quadric equations, making the calculation of slicing and path planning easier. With these equations, we can deduce the spatial mapping functions. In this section, firstly, we introduce the intersection between the

**Figure 2** An overhang sliced by the equidistant surface of the original surface



triangle-meshed 3D model and a cylindrical or conical surface; secondly, the path planning method on cylindrical or conical surfaces is presented.

### 2.1 The intersection between cylindrical or conical surfaces and the object's surface

To simplify the calculation of slicing, we propose a unit equation for cylindrical and conical surfaces. A conical surface can be transferred to a cylindrical surface when its taper angle infinitely approaches to zero. Knowing the radius  $R$  and the height  $H$  of the conical surface, it can be represented by one quadric surface equation as follows:

$$x^2 + y^2 = R^2 \left( \frac{z}{H} - 1 \right)^2 \quad (1)$$

Equation (1) can describe cylindrical surface when  $H \rightarrow \infty$ . In the following, we use a conical surface to represent both the cylindrical surface and the conical surface.

The question of the intersection between the triangle-meshed 3D model and a conical surface can be divided into the question of intersections between triangle facets and the conical surface, and the question of merging intersecting lines into paths.

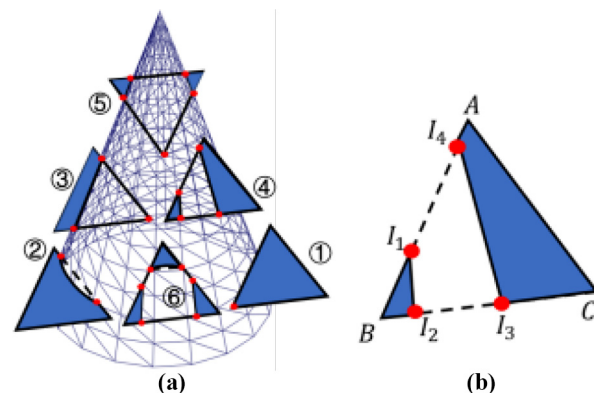
#### 2.1.1 Intersections between triangle facets and the conical surface

As a quadric surface, a conical surface mostly has two intersecting points with an edge, except the case when the edge is on a generatrix of the conical surface. If an edge is on a generatrix, the endpoints of the edge are regarded as the two intersecting points. After the intersection, there will be mostly six intersecting points on three edges of a facet. Figure 3(a) shows the intersections between the conical surface and triangle facets with the number of intersecting points ranging from 1 to 6.

The intersecting points between an edge and the conical surface are calculated as follows. Given the endpoints  $p_0 (x_0, y_0, z_0)$  and  $p_1 (x_1, y_1, z_1)$  of an edge, the intersecting point  $I(x, y, z)$  can be described with a parametric equation of  $t$ :

$$(x, y, z) = t(x_1, y_1, z_1) + (1 - t)(x_0, y_0, z_0) \quad (2)$$

**Figure 3** (a) Intersections between the conical surface and triangle facets; (b) Intersecting segments  $I_1I_2$  and  $I_3I_4$



With equation (1) and equation (2), we can get two solutions of  $t$ . If  $0 \leq t \leq 1$ , there must exist at least one intersecting point between the edge and the conical surface.

According to the number of intersecting segments of the intersection between a triangle facet and the conical surface, the intersection can be classified into three cases, from one segment to three segments. Each intersecting segment has two intersecting points, which are linked with a straight line to approach the intersecting curve, as you can see in Figure 3(a) ②, ④ and ⑥, where the straight lines are drawn in imaginary lines. Let us have a look at these three cases:

- 1 There is only one segment. The endpoints could be on the same edge as shown in Figure 3(a) ②, or on different edges as shown in Figure 3(a) ③.
- 2 There are two segments. The endpoints of either segment locate on different edges as shown in Figure 3(a) ④ and ⑤.
- 2 **Proof:** As we can see in Figure 3(b),  $I_1, I_2, I_3$  and  $I_4$  are the four endpoints. Edge  $AB$  is divided by the conical surface into three segments,  $I_1I_4, AI_4$  and  $I_1B$ , while edge  $BC$  is divided into  $I_2I_3, BI_2$  and  $I_3C$ .  $I_1B, BI_2, AI_4$ , and  $I_3C$  are outside the surface, while  $I_1I_4$  and  $I_2I_3$  are inside the surface. Then we have triangle  $BI_1I_2$  and quadrangle  $AI_4I_3C$  outside the surface, while quadrangle  $I_1I_2I_3I_4$  inside the surface. So  $I_1I_2$  and  $I_3I_4$  are the dividing segments.
- 3 There are three segments. The endpoints of any segment should be on different edges as shown in Figure 3(a) ⑥. It can be proved as above.

### 2.1.2 Merging intersecting lines into paths

The intersecting lines are merged into several contiguous contours through the following five steps:

- 1 **Step 0** For any facet, delete the intersecting points on vertexes, then the number of intersecting points could be 2, 4 or 6. These points are grouped into pairs by two criterions: these pairs should not cross and a pair of points locate on different edges:
- 2 **Step 1** Pick one intersecting point  $v_1$  as a start and push it into a path  $p_1$ ;  $p_1 = \{v_1\}$ .
- 3 **Step 2** For the last point  $v_i$  of this path, execute Step 3 in a loop until the second point is  $v_1$ , meaning all the points on a curve have been traversed.
- 4 **Step 3** For the facet where  $v_i$  locates, calculate the number  $n$  of intersecting points. If  $n = 2$ , find the second point  $v_2$  and push it into this path. If  $n = 4$  or 6, find the second point  $v_2$  of the same pair of  $v_1$  and push it into this path.
- 5 **Step 4** If there are intersecting points having not been pushed into  $p_1$ , pick one point from these points as a start and push it into a new path  $p_j$  ( $j = 2, 3, 4, \dots$ ), and execute Step 2 in a loop until all the intersecting points having been linked.

### 2.2 Path planning on conical surfaces

A set of contours are generated when the model is sliced by equidistant developable surfaces. These contours can be flattened onto a plane, where filling paths are generated. Figure 4 illustrates the path planning on a conical surface, including three steps: firstly, mapping the contours from conical surfaces to planes by surface flattening; secondly,

creating filling paths; thirdly, mapping the filling paths back to the conical surface. In the first step, the conical surface is cut open through a generatrix, called **cutting line**. It should be noted that when the cutting line intersects with the contour, the contour should be rotated around the center axis of the cone by a certain angle  $\alpha$ , or it would be broken up after being mapped to planes. At the end of the process, rotate the paths by an angle  $-\alpha$ . In this case, before mapped to planes, a point  $P(x_0, y_0, z_0)$  on the surface is multiplied by a certain rotating matrix:

$$(x'_0, y'_0, z'_0)^{-1} = \begin{bmatrix} \cos\alpha & \sin\alpha & 0 \\ -\sin\alpha & \cos\alpha & 0 \\ 0 & 0 & 1 \end{bmatrix} (x_0, y_0, z_0)^{-1}.$$

After mapped from planes to surfaces, the point  $P_1(x_1, y_1, z_1)$  is multiplied by an inverse rotating matrix:

$$(x'_1, y'_1, z'_1)^{-1} = \begin{bmatrix} \cos\alpha & -\sin\alpha & 0 \\ \sin\alpha & \cos\alpha & 0 \\ 0 & 0 & 1 \end{bmatrix} (x_1, y_1, z_1)^{-1}.$$

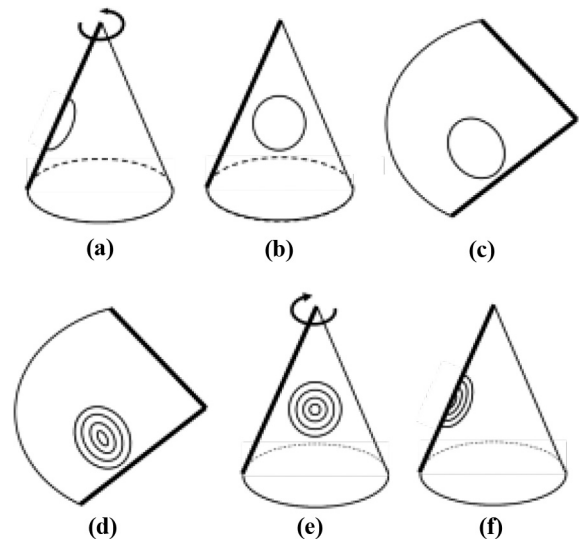
We took an iterating method to find an available  $\alpha$  by setting a certain degree (we use  $11^\circ$  in this paper) then testing whether it is available. If not, we proceed to multiple the degree ( $22^\circ, 33^\circ, 44^\circ$  and so on) until it is available.

Figure 5 illustrates the transformation of conical surface flattening. The conical surface is cut open through cutting line  $OB$  ( $O$  is the cone vertex) and rotated around  $O$  until point  $A$  coming to point  $A_1$  on the  $x$ -axis, then spread from  $OA_1$ . After being flattened from the 3D coordinate system  $O_{cone}xyz$ , there is a sector expansion on a 2D coordinate system  $Oxy$ .

For a given point  $P_0(x_0, y_0, z_0)$  on the conical surface, it can be represented by:

$$x_0 = \frac{-z_0}{H} R \cos\theta_0$$

Figure 4 Path planning on a conical surface



**Notes:** (a) The contour intersecting with the cutting line; (b) the contour after rotation; (c) the contour flattened onto a plane; (d) the filling paths of the contour on the plane; (e) the filling paths mapped back to the conical surface; (f) the final filling paths after rotation



$$y_0 = \frac{-z_0}{H} R \sin \theta_0$$

where  $\theta_0 = \text{atan2}(y_0, x_0)$ .

$d\theta_0$ ,  $d\theta$ , and  $dS$  represent tiny values added to  $\theta_0$ ,  $\theta$  (the spreading angle from  $OA$  to  $OC$ ) and  $S$  (the length of elliptical arc  $AC$ ) respectively.  $dS$ , as a tiny arc of the ellipse on the undersurface,  $dS \approx \sqrt{(aR \cos \theta_0)^2 + (bR \sin \theta_0)^2} d\theta_0$  or a tiny arc of the sector on the conical surface,  $dS \approx \sqrt{(aR \cos \theta)^2 + (bR \sin \theta)^2 + H^2} d\theta$ . Let  $d\theta_0 \rightarrow 0$ ,  $d\theta \rightarrow 0$ . The following integrations show the relations between  $\theta$  and  $\theta_0$ :

$$\theta = \int \frac{\sqrt{(R \cos \theta_0)^2 + (R \sin \theta_0)^2}}{\sqrt{(R \cos \theta)^2 + (R \sin \theta)^2 + H^2}} d\theta_0 = \frac{R \theta_0}{\sqrt{R^2 + H^2}}$$

It can be deduced that the function mapping the point  $P_0(x_0, y_0, z_0)$  on the conical surface to a point  $P(x, y)$  on plane is:

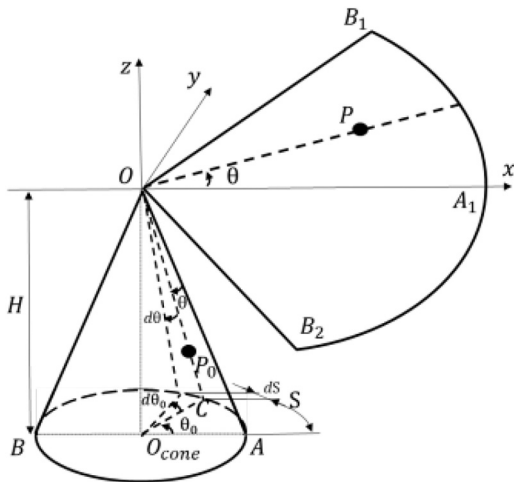
$$(x, y)^{-1} = \begin{pmatrix} \cos \left[ \frac{R}{\sqrt{R^2 + H^2}} (\text{atan2}(y_0, x_0)) \right] \sqrt{\left( R \frac{H - z_0}{H} \right)^2 + (H - z_0)^2} \\ \sin \left[ \frac{R}{\sqrt{R^2 + H^2}} (\text{atan2}(y_0, x_0)) \right] \sqrt{\left( R \frac{H - z_0}{H} \right)^2 + (H - z_0)^2} \end{pmatrix}$$

and the function mapping the point  $P(x, y)$  on plane to a point  $P_0(x_0, y_0, z_0)$  on the conical surface is:

$$(x_1, y_1, z_1)^{-1} = \begin{pmatrix} \cos \left[ \frac{\sqrt{R^2 + H^2}}{R} (\text{atan2}(y, x)) \right] (-z_1) R / H \\ \sin \left[ \frac{\sqrt{R^2 + H^2}}{R} (\text{atan2}(y, x)) \right] (-z_1) R / H \\ - \frac{H \sqrt{x^2 + y^2}}{\sqrt{R^2 + H^2}} \end{pmatrix}$$

For a better integrality, we illustrate the conventional path filling formats for a planer contour. The contours are filled with

**Figure 5** The transformation of conical surface flattening

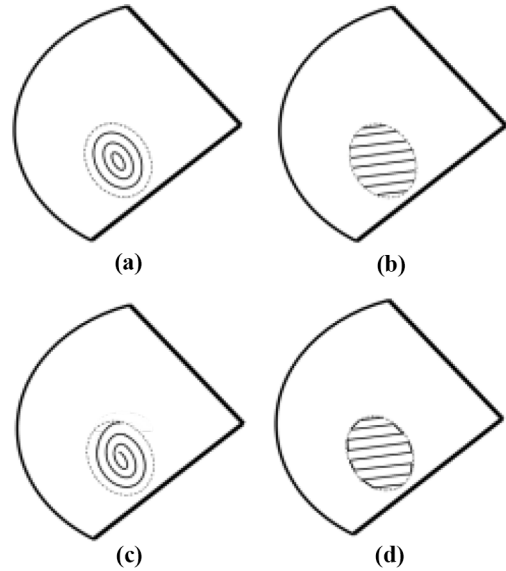


parallel contours as shown in Figure 6(a) or parallel lines as shown in Figure 6(b). For better continuity, the filling paths can be linked with short arcs or lines, thus generating a consecutive spiral line as shown in Figure 6(c) or zigzag line as shown in Figure 6(d).

### 3. Five-axis algorithm

The five-axis process can be realized by rotating the part via two-axis turntable to orientate the surface normal toward the weld torch. During the rotation, any point  $P_1$  on the original too-paths will get to a new position  $P_1'$  (Figure 7). In this

**Figure 6** Four path filling formats on planes



**Notes:** (a) Parallel contours; (b) parallel lines; (c) spiral lines; (d) zigzag lines

**Figure 7** Five-axis transformation

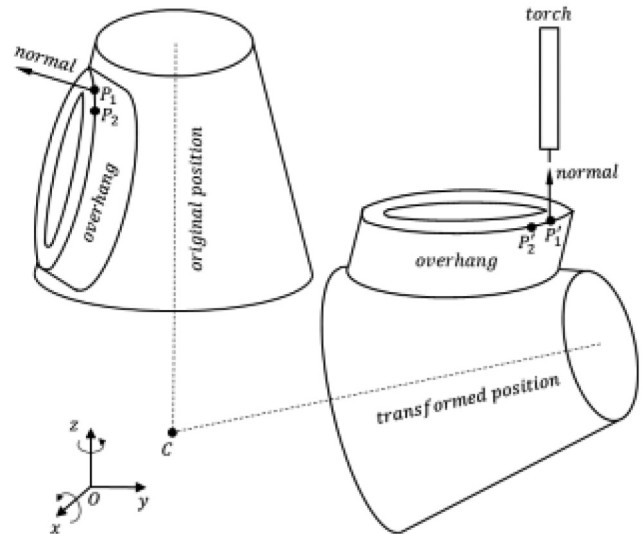


**Figure 8** Rotations of two sequential points

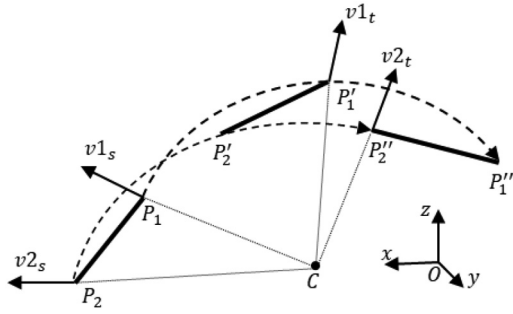


**Figure 9** Three transforming steps of the rotation

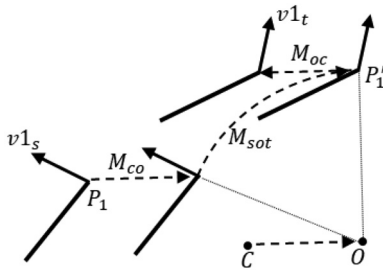
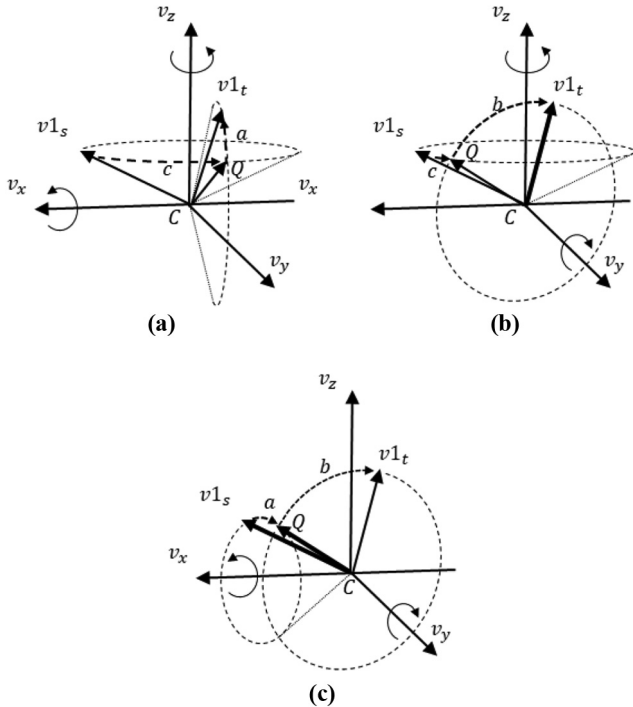


**Figure 10** Rotation from  $v1_s$  to  $v1_t$  around two vectors



**Notes:** (a) Rotation around  $v_x$  and  $v_z$ ; (b) rotation around  $v_y$  and  $v_z$ ; (c) Rotation around  $v_x$  and  $v_y$

section, we will give mathematical solutions for the calculation of five-axis transformation.

Given 2 sequential points  $P_1$  and  $P_2$  on a path, fixed with vectors  $v1_s$  and  $v2_s$  respectively, which have been normalized. Rotating these two points around center point  $C(X_C, Y_C, Z_C)$ , after the first rotation we get points  $P'_1$  from  $P_1$ ,  $P'_2$  from  $P_2$  and vector  $v1_t$  from  $v1_s$ , after the second rotation we get points  $P''_1$  from  $P'_1$ ,  $P''_2$  from  $P'_2$  and vector  $v2_t$  from  $v2_s$  shown in Figure 8.

If the rotation is performed via two of these three vectors  $v_x(1,0,0)$ ,  $v_y(0,1,0)$  and  $v_z(0,0,1)$ , the question can be described as:

Known  $P_1(X_{P_1}, Y_{P_1}, Z_{P_1})$ ,  $v1_s(X_{v1_s}, Y_{v1_s}, Z_{v1_s})$  and  $v1_t(X_{v1_t}, Y_{v1_t}, Z_{v1_t})$ , calculate  $P'_1(X_{P'_1}, Y_{P'_1}, Z_{P'_1})$  and the rotating angles around two vectors of  $v_x(1,0,0)$ ,  $v_y(0,1,0)$  and  $v_z(0,0,1)$ .

After the transformation, we have  $P'_1 = M_{st} * P_1$ , where  $M_{st}$  is the transformation matrix. In the following, two solutions are given. Solution 1 takes no consideration of the usable axes of the five-axis platform. Solution 2 takes it into consideration.

### 3.1 Solution 1

Rotating  $v1_s$  to  $v1_t$  around  $C$ , includes three steps: translating from  $v1_s C$  to  $O$ , then rotating  $v1_s$  to  $v1_t$  around  $O$ , and translating  $v1_s$  from  $O$  to  $C$ , shown in Figure 9, corresponding to three transformation matrixes  $M_{co}$ ,  $M_{sot}$  and  $M_{oc}$  respectively, written as  $M_{st} = M_{co} * M_{sot} * M_{oc}$ . The translation matrixes  $M_{co}$  and  $M_{oc}$  can be represented as

$$M_{co} = \begin{bmatrix} 1 & 0 & 0 & -X_C \\ 0 & 1 & 0 & -Y_C \\ 0 & 0 & 1 & -Z_C \\ 0 & 0 & 0 & 1 \end{bmatrix} \quad M_{oc} = \begin{bmatrix} 1 & 0 & 0 & X_C \\ 0 & 1 & 0 & Y_C \\ 0 & 0 & 1 & Z_C \\ 0 & 0 & 0 & 1 \end{bmatrix}, \quad \text{while}$$

rotating matrix  $M_{sot}$  is equal to the result of rotating around vectors  $v_z$ ,  $v_y$  and  $v_x$  by angles  $c$ ,  $b$  and  $a$ , respectively, represented as

$$M_{sot} = \begin{bmatrix} 1 & 0 & 0 & 0 \\ 0 & \cos a & -\sin a & 0 \\ 0 & \sin a & \cos a & 0 \\ 0 & 0 & 0 & 1 \end{bmatrix} * \begin{bmatrix} \cos b & 0 & \sin b & 0 \\ 0 & 1 & 0 & 0 \\ -\sin b & 0 & \cos b & 0 \\ 0 & 0 & 0 & 1 \end{bmatrix} * \begin{bmatrix} \cos c & -\sin c & 0 & 0 \\ \sin c & \cos c & 0 & 0 \\ 0 & 0 & 1 & 0 \\ 0 & 0 & 0 & 1 \end{bmatrix}$$

. Thus, we have  $P'_1 = M_{co} * M_{sot} * M_{oc} * P_1$ , specifically,

$$P'_1 = \begin{bmatrix} 1 & 0 & 0 & X_C \\ 0 & 1 & 0 & Y_C \\ 0 & 0 & 1 & Z_C \\ 0 & 0 & 0 & 1 \end{bmatrix} * \begin{bmatrix} 1 & 0 & 0 & 0 \\ 0 & \cos a & -\sin a & 0 \\ 0 & \sin a & \cos a & 0 \\ 0 & 0 & 0 & 1 \end{bmatrix} * \begin{bmatrix} \cos b & 0 & \sin b & 0 \\ 0 & 1 & 0 & 0 \\ -\sin b & 0 & \cos b & 0 \\ 0 & 0 & 0 & 1 \end{bmatrix} * \begin{bmatrix} \cos c & -\sin c & 0 & 0 \\ \sin c & \cos c & 0 & 0 \\ 0 & 0 & 1 & 0 \\ 0 & 0 & 0 & 1 \end{bmatrix} * \begin{bmatrix} 1 & 0 & 0 & -X_C \\ 0 & 1 & 0 & -Y_C \\ 0 & 0 & 1 & -Z_C \\ 0 & 0 & 0 & 1 \end{bmatrix} * P_1 \quad (3)$$

To calculate  $M_{soz}$ , we should look at the second step of the transformation. The second step, rotating  $v_{1s}$  to  $v_{1t}$  around  $O$ , is able to be carried out via two vectors of  $v_x$ ,  $v_y$ , and  $v_z$ , which is proved in the following.

As shown in Figure 10,  $v_{1s}$  is rotated to  $v_{1t}$  by rotating  $v_{1s}$  to vector  $CQ$  ( $X_Q, Y_Q, Z_Q$ ) via one axis, then rotating  $CQ$  to  $v_{1t}$  via another axis.

If we choose  $v_x$  and  $v_z$  as axes in Figure 10(a), we have:

$$X_Q = X_{v1_t}$$

$$Z_Q = Z_{v1_t}$$

$$Y_Q = \pm \sqrt{1 - X_{v1_t}^2 - Z_{v1_t}^2}$$

$$c = \text{atan2}(Y_Q, X_Q) - \text{atan2}(Y_{v1_t}, X_{v1_t})$$

$$b = 0$$

$$a = \text{atan2}(Z_{v1_t}, Y_{v1_t}) - \text{atan2}(Z_Q, Y_Q)$$

There is no real solution if  $X_{v1_t}^2 + Z_{v1_t}^2 > 1$ .

If we choose  $v_y$  and  $v_z$  as axes in Figure 10(b), or  $v_x$  and  $v_y$  as axes in Figure 10(c), we will get similar result.

There must be at least one real solution, because  $(X_{v1_t}^2 + Z_{v1_t}^2) + (Y_{v1_t}^2 + Z_{v1_t}^2) + (Y_{v1_t}^2 + Z_{v1_t}^2) \neq 3$ . Then it is proved that  $v_{1s}$  can be rotated around  $O$  to  $v_{1t}$  via 2 vectors of  $v_x$ ,  $v_y$ , and  $v_z$ . We can get  $P'_1(X_{P'_1}, Y_{P'_1}, Z_{P'_1})$  when putting the values of  $c$ ,  $b$  and  $a$  into equation (3). However, the five-axis platform may not have these two rotating axes.

### 3.2 Solution 2

Solution 1 tells us that, there could be no real solutions when rotating  $v_{1s}$  to  $v_{1t}$  via two axes of  $v_x$ ,  $v_y$ , and  $v_z$ , so a vector  $v_z(0,0,1)$  is introduced as a transition, shown in Figure 11, where  $v_{1s}$  is firstly transformed to  $v_z$ . The transformation matrixes rotating around  $C$  from  $v_{1s}$  to  $v_z$  and from  $v_z$  to  $v_{1t}$  are  $M_{sz}$  and  $M_{zt}$  respectively. We can get  $M_{st}$  by multiplying  $M_{sz}$  and  $M_{zt}$ , there is  $M_{st} = M_{sz} * M_{zt}$ .

We first deal with the problem of rotating  $v_{1s}$  to  $v_z$  around  $C$ , which has such three steps, translating from  $C$  to  $O$ , then rotating  $v_{1s}$  to  $v_z$  around  $O$ , and translating from  $O$  to  $C$ , corresponding to three transformation matrixes,  $M_{co}$ ,  $M_{soz}$  and  $M_{oc}$  respectively, while rotating matrix  $M_{soz}$  is equal to the matrixes of rotating around  $v_z(1,0,0)$ ,  $v_y(0,1,0)$  and  $v_x(0,0,1)$  by angles  $\gamma$ ,  $\beta$  and  $\alpha$  respectively, thus we have:

$$M_{sz} = \begin{bmatrix} 1 & 0 & 0 & X_C \\ 0 & 1 & 0 & Y_C \\ 0 & 0 & 1 & Z_C \\ 0 & 0 & 0 & 1 \end{bmatrix} * \begin{bmatrix} 1 & 0 & 0 & 0 \\ 0 & \cos\alpha & -\sin\alpha & 0 \\ 0 & \sin\alpha & \cos\alpha & 0 \\ 0 & 0 & 0 & 1 \end{bmatrix}$$

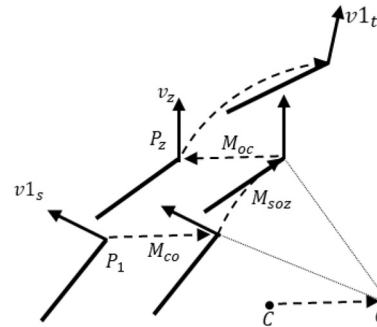
$$* \begin{bmatrix} \cos\beta & 0 & \sin\beta & 0 \\ 0 & 1 & 0 & 0 \\ -\sin\beta & 0 & \cos\beta & 0 \\ 0 & 0 & 0 & 1 \end{bmatrix} * \begin{bmatrix} \cos\gamma & -\sin\gamma & 0 & 0 \\ \sin\gamma & \cos\gamma & 0 & 0 \\ 0 & 0 & 1 & 0 \\ 0 & 0 & 0 & 1 \end{bmatrix}$$

$$* \begin{bmatrix} 1 & 0 & 0 & -X_C \\ 0 & 1 & 0 & -Y_C \\ 0 & 0 & 1 & -Z_C \\ 0 & 0 & 0 & 1 \end{bmatrix} \quad (4)$$

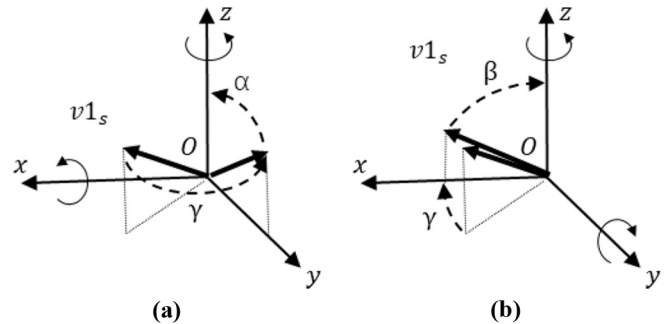
To calculate  $M_{soz}$ , look at the second step.  $v_{1s}$  can be rotated to  $v_z$  through mere two axes. Here we choose the  $x$ -axis and  $z$ -axis as an example shown in Figure 12(a), firstly rotating  $v_{1s}$  around the  $z$ -axis by  $\gamma$  until it is on  $yOz$  plane and then rotating around  $x$ -axis to  $v_z$  by  $\alpha$ .  $\tan(\gamma) = \frac{Y_{v1_s}}{X_{v1_s}}$ ,  $\cos(\alpha) = \frac{Z_{v1_t}}{\sqrt{X_{v1_s}^2 + Y_{v1_s}^2 + Z_{v1_s}^2}} = Z_{v1_s}$ . By rotating  $v_{1s}$  around the  $z$ -axis,  $y$ -axis and  $x$ -axis successively, we get  $\gamma = \text{atan2}(Y_{v1_s}, X_{v1_s})$ ,  $\beta = 0$ ,  $\alpha = \text{acos}(Z_{v1_s})$ . It is similar if we choose the  $y$ -axis and  $z$ -axis shown in Figure 12(b).

As for  $M_{zt}$  in the process of rotating  $v_z$  to  $v_{1t}$  around  $C$ , it can be written as  $M_{zt} = M_{co} * M_{zot} * M_{oc}$ , where  $M_{zot}$  is the rotating matrix from  $v_z$  to  $v_{1t}$  around  $O$ . As an inverse process of rotating  $v_{1t}$  to  $v_z$  around  $O$ , it can be performed by rotating around  $x$ -axis,  $y$ -axis and  $z$ -axis by angles  $\alpha'$ ,  $\beta'$  and  $\gamma'$  respectively, presented as follows:

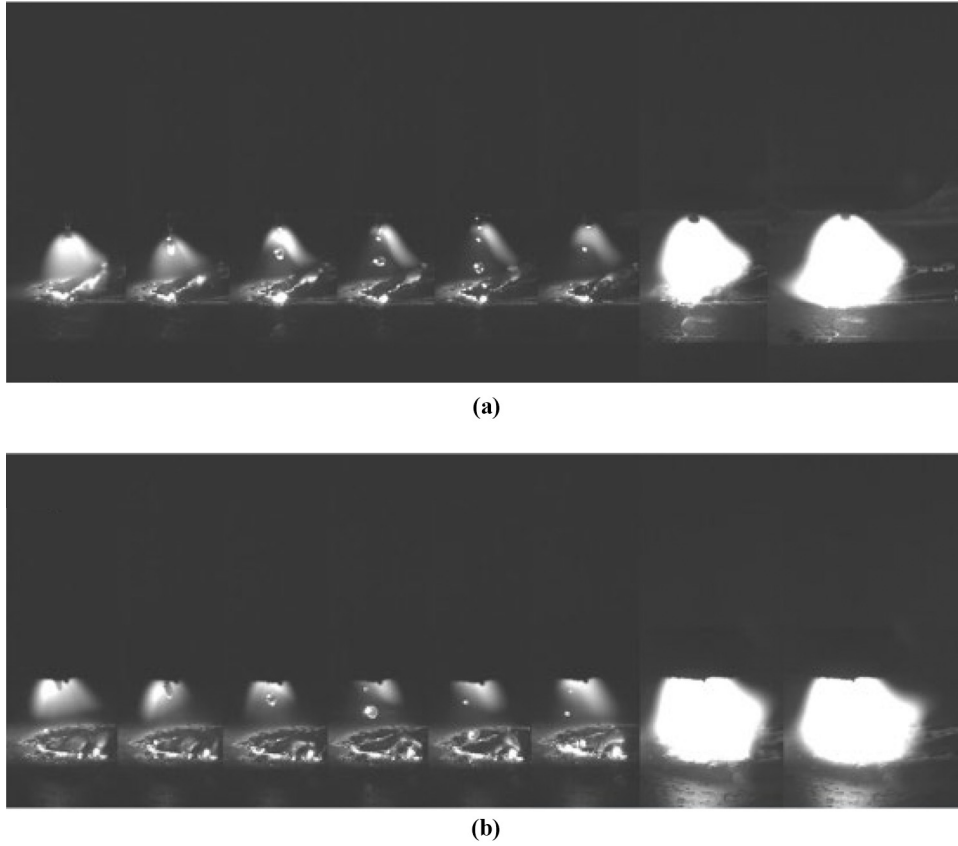
**Figure 11** Vector  $v_z(0,0,1)$  introduced as a transition of the transformation



**Figure 12** Transformation to  $v_z(0,0,1)$  via two axes



**Notes:** (a) Transformation via  $x$ -axis and  $z$ -axis; (b) transformation via  $y$ -axis and  $z$ -axis

**Figure 13** Pictures of the arc shape and the droplet transfer under different curvature**Notes:** (a) The curvature 1/1 (a line); (b) the curvature 1/30 (a circle with a radius of 30 mm)

$$M_{\text{rot}} = \begin{bmatrix} \cos \gamma' & -\sin \gamma' & 0 & 0 \\ \sin \gamma' & \cos \gamma' & 0 & 0 \\ 0 & 0 & 1 & 0 \\ 0 & 0 & 0 & 1 \end{bmatrix} * \begin{bmatrix} \cos \beta' & 0 & \sin \beta' & 0 \\ 0 & 1 & 0 & 0 \\ -\sin \beta' & 0 & \cos \beta' & 0 \\ 0 & 0 & 0 & 1 \end{bmatrix} * \begin{bmatrix} 1 & 0 & 0 & 0 \\ 0 & \cos \alpha' & -\sin \alpha' & 0 \\ 0 & \sin \alpha' & \cos \alpha' & 0 \\ 0 & 0 & 0 & 1 \end{bmatrix} \quad (5)$$

where

$$\alpha' = -\arccos(Z_{v1_i})$$

$$\beta' = 0$$

$$\gamma' = -\arctan2(Y_{v1_i}, X_{v1_i})$$

The whole transformation is achieved by merging these two processes, then we have  $P'_1 = (M_{co} * M_{s0z} * M_{oc}) * (M_{co} * M_{\text{rot}} * M_{oc}) * P_1 = M_{co} * M_{s0z} * M_{\text{rot}} * M_{oc} * P_1$ . With [equation \(4\)](#) and [equation \(5\)](#), we get the second solution:

$$P_1 = \begin{bmatrix} 1 & 0 & 0 & X_C \\ 0 & 1 & 0 & Y_C \\ 0 & 0 & 1 & Z_C \\ 0 & 0 & 0 & 1 \end{bmatrix} * \begin{bmatrix} 1 & 0 & 0 & 0 \\ 0 & \cos \alpha & -\sin \alpha & 0 \\ 0 & \sin \alpha & \cos \alpha & 0 \\ 0 & 0 & 0 & 1 \end{bmatrix} * \begin{bmatrix} \cos \beta & 0 & \sin \beta & 0 \\ 0 & 1 & 0 & 0 \\ -\sin \beta & 0 & \cos \beta & 0 \\ 0 & 0 & 0 & 1 \end{bmatrix} * \begin{bmatrix} \cos \gamma & -\sin \gamma & 0 & 0 \\ \sin \gamma & \cos \gamma & 0 & 0 \\ 0 & 0 & 1 & 0 \\ 0 & 0 & 0 & 1 \end{bmatrix} * \begin{bmatrix} \cos \beta' & 0 & \sin \beta' & 0 \\ 0 & 1 & 0 & 0 \\ -\sin \beta' & 0 & \cos \beta' & 0 \\ 0 & 0 & 0 & 1 \end{bmatrix} * \begin{bmatrix} 1 & 0 & 0 & 0 \\ 0 & \cos \alpha' & -\sin \alpha' & 0 \\ 0 & \sin \alpha' & \cos \alpha' & 0 \\ 0 & 0 & 0 & 1 \end{bmatrix} * \begin{bmatrix} 1 & 0 & 0 & -X_C \\ 0 & 1 & 0 & -Y_C \\ 0 & 0 & 1 & -Z_C \\ 0 & 0 & 0 & 1 \end{bmatrix}$$



where

$$\alpha = \arccos(Z_{v1_i})$$

$$\beta = 0$$

$$\gamma = \arctan2(Y_{v1_i}, X_{v1_i})$$

$$\alpha' = -\arccos(Z_{v1_i})$$

$$\beta' = 0$$

$$\gamma' = -\arctan2(Y_{v1_i}, X_{v1_i})$$

Coming here, the absolute velocity  $V_s$  from  $P_1'$  to  $P_2''$  in coordinate  $Oxyz$  can be calculated. Knowing  $P_2$  ( $X_{P_2}, Y_{P_2}, Z_{P_2}$ ),  $v_{2s}$  ( $X_{v2_s}, Y_{v2_s}, Z_{v2_s}$ ) and  $v_{2t}$  ( $X_{v2_t}, Y_{v2_t}, Z_{v2_t}$ ), it is easy to calculate  $P_2''$  ( $X_{P_2''}, Y_{P_2''}, Z_{P_2''}$ ). The length between

$P_1'$  and  $P_2''$  is  $|P_1'P_2''|$ . The time it spends from  $P_1'$  to  $P_2''$  is  $T = \frac{|P_1'P_2|}{V}$ . The average velocity from  $P_1'$  to  $P_2''$  in coordinate  $Oxyz$  is  $V_s = \frac{|P_1'P_2|}{T} = \frac{|P_1'P_2| * V}{|P_1'P_2|}$ .

**Figure 14** The magnetic field and electromagnetic forces around the arc

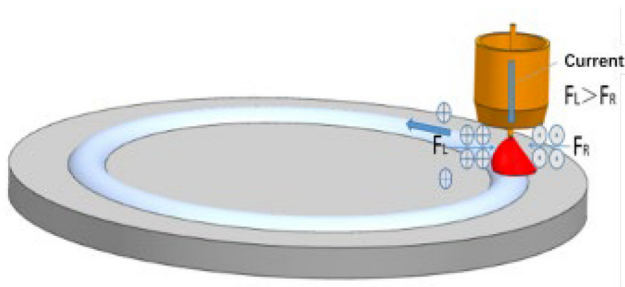
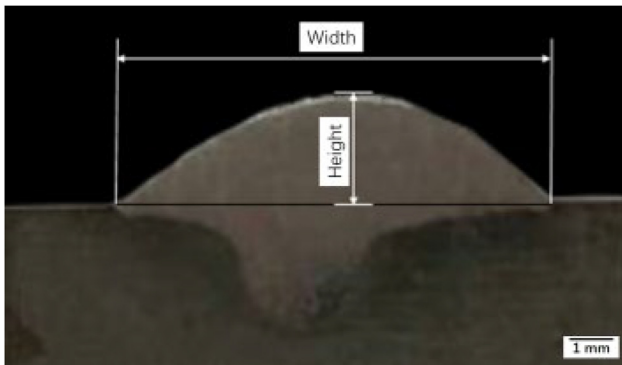


**Figure 15** Cross section of a bead



## 4. Experiments

As the tool-paths on a conical surface or a cylindrical surface can be transformed onto a flat surface, we suppose that the planar welding process is useful for the welding on a conical surface or a cylindrical surface. In the following, we will introduce the study about the influence of the curvature of the tool-path and the travel speed on the surface appearance of the welding beads, then apply the result on a conical surface and a cylindrical surface.

The shape of the tool-path has a great influence on the surface appearance of the welding beads in WAAM. To figure out the influence of the curvature, we have taken pictures of the arc shape and the droplet transfer under different curvature using the high-speed camera PELICAN 1560 CASE. The camera was fixed right behind the welding gun along the tool-path, and the traveling of the welding gun was achieved by rotating the rotary table. Keeping other parameters unchanged, we took eight pictures as a group in one pulse period during the deposition, shown in Figure 13. When the path is a line (the curvature is  $1/\infty$ ), the arc is basically shaped in a Gaussian distribution (Figure 13(a)). When the path is a circle (the curvature is  $1/30$ ), the arc in the inner side of the circle contracts to some extent, with big drop repulsion transition (Figure 13(b)).

According to the basic theory of electromagnetism, we know that the welding arc is a flexible gas conductor between electrode and molten pool, with the magnetic field

**Table 1** Experiment scheme and results

No.	Curvature radius (mm)	Wire feeding speed (m/min)	Travel speed (mm/min)	Width (mm)	Height (mm)
1	30	6.5	300	12.52	3.40
2	30	6.5	600	9.86	2.68
3	30	6.5	900	9.14	2.52
4	50	6.5	300	12.44	3.26
5	50	6.5	600	9.46	2.50
6	50	6.5	900	8.28	2.44
7	70	6.5	300	12.10	3.12
8	70	6.5	600	9.22	2.52
9	70	6.5	900	8.00	2.34
10	90	6.5	300	11.34	3.34
11	90	6.5	600	8.72	2.42
12	90	6.5	900	7.46	2.14

around. The magnetic field is generated not only from the wire and arc, but also from the welding bead. When the fusion model is completely symmetric, the center current has no lateral deflection, so the axial electromagnetic force is zero (Xie *et al.*, 2015). When the fusion model is asymmetric, the magnetic field is in asymmetric distribution around the arc, where the magnetic induction linear density is smaller in the inner side and larger in the outer side. Thus, the center current has some lateral deflection to the outer side. Figure 14 shows the electromagnetic forces  $F_L$  and  $F_R$  generated by the magnetic fields on both sides. The magnetic bias forces the arc to deflect.

To avoid interfering factors, we set the shielding gas flow rate at 18 L/min, the gun plate spacing at 10 mm and the wire feeding speed at 6.5 m/min, and keep the gun vertical to the plate. To investigate the influence of the curvature on the welding appearance, specifically, the width and height, we have acquired welding beads with different curvatures and travel speeds. Each bead was cut along cross section at three different positions. The width and height of a polished sample are shown in Figure 15. The width and height of a bead are the averages of those of the three samples. Figure 15 shows that the top of the bead has

lateral deflection relative to the bottom, which is in accord with the deflection of the arc shape. The experiment scheme and result are shown in Table 1.

We find that in Figure 16, at the same travel speed, the larger the radius of curvature is, the smaller the width of the bead would be. When the curvature radius tends to be infinite, the width would tend to be constant. Suppose that:

$$w = \frac{p}{r} + q \quad (6)$$

where  $w$  is the width, and  $r$  is the curvature radius.

Meanwhile, the width of the bead gets smaller when the travel speed gets larger. To investigate the influence of the travel speed  $v$  on the width  $w$ , we look at their relationships with the bead area  $A$ . The profile of a single bead can be fitted with a parabola or a hyperbola (Ding *et al.*, 2016), written as  $f(x) = ax^2 + bx + h$ , where  $x \in [-\frac{w}{2}, \frac{w}{2}]$ ,  $h$  is the height of the bead. We have:

$$f\left(\frac{w}{2}\right) = 0 \quad (7)$$

The bead area is the integration of  $f(x)$  on  $[-\frac{w}{2}, \frac{w}{2}]$ :

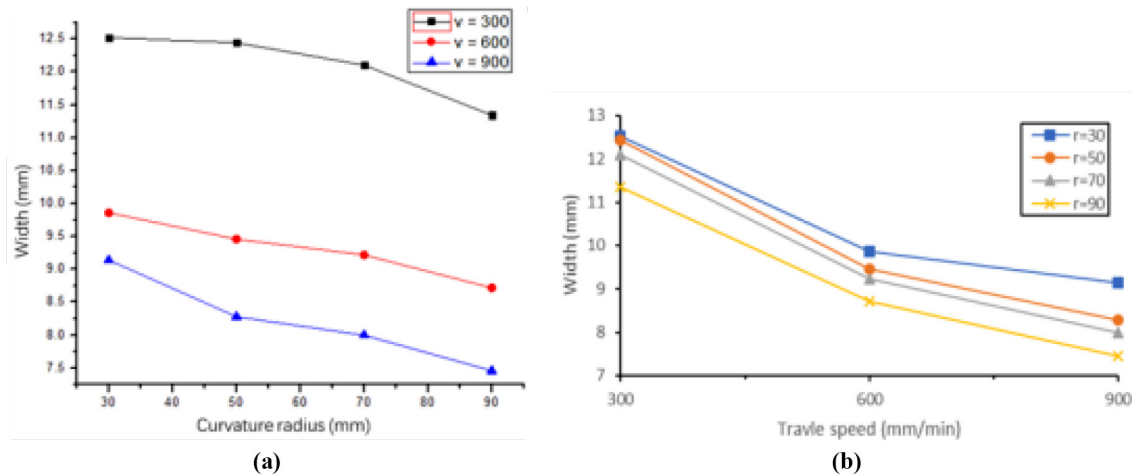
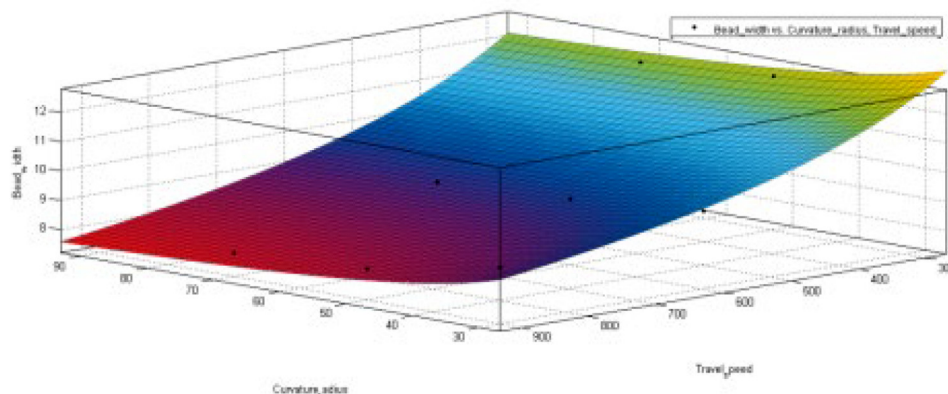
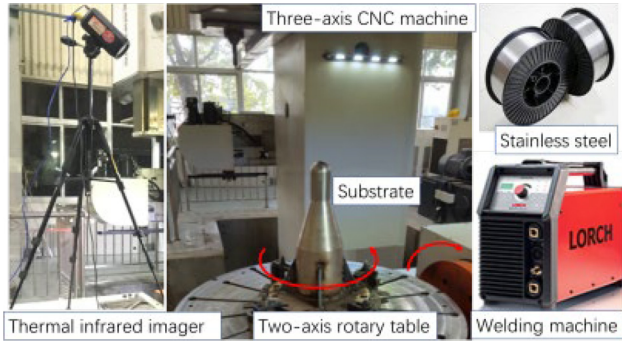


Figure 17 Regression fitting surface of the bead width as the function of the curvature radius and welding travel speed



$$A = \int_{-\frac{\pi}{2}}^{\frac{\pi}{2}} f(x) dx \quad (8)$$

**Figure 18** Experimental setup



**Figure 19** Tool-paths on a conical surface

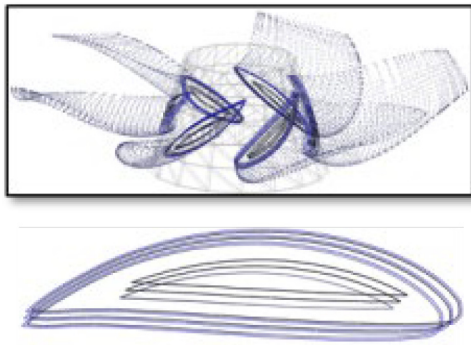
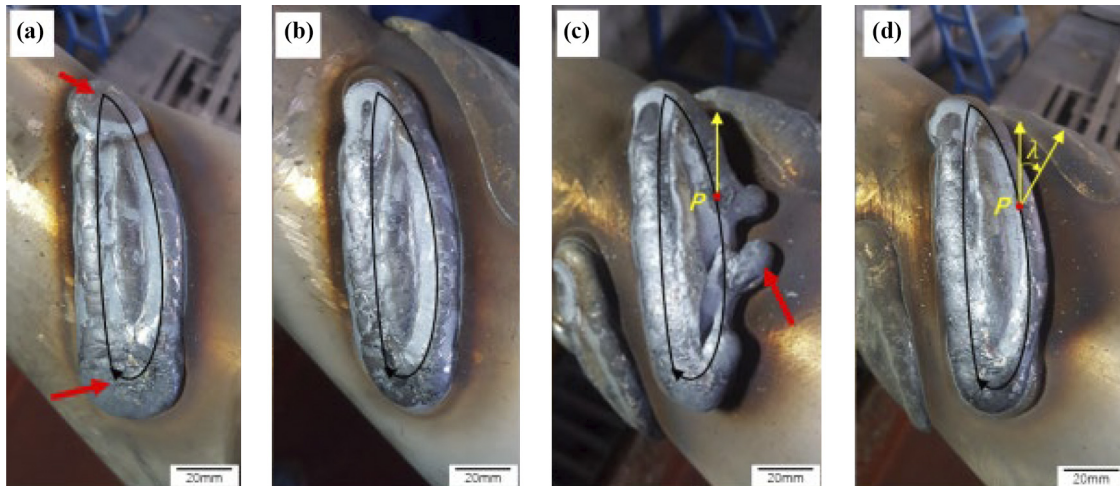


**Figure 20** Weld beads printed on conical surface



**Notes:** (a) Beads of the first layer using a constant travel speed; (b) beads of the first layer using CSW model; (c) beads of the second layer; (d) beads of the second layer with orientation deflecting on contour

What is more, the bead area is inversely proportional to the travel speed (Ding *et al.*, 2016):

$$A = \frac{k}{v} \quad (9)$$

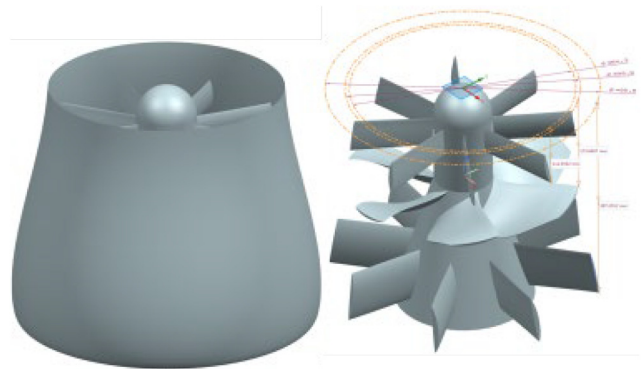
With equations (7) (8) and (9), we have  $k_0 w^3 + k_1 w^2 + k_2 w + k_3 = v^{-1}$ . Leave out the low order terms, we have the approximate equation:

$$w = mv^{-\frac{1}{3}} + n \quad (10)$$

With equations (6) and (10), we can construct the following model of  $w$ ,  $r$  and  $v$ :

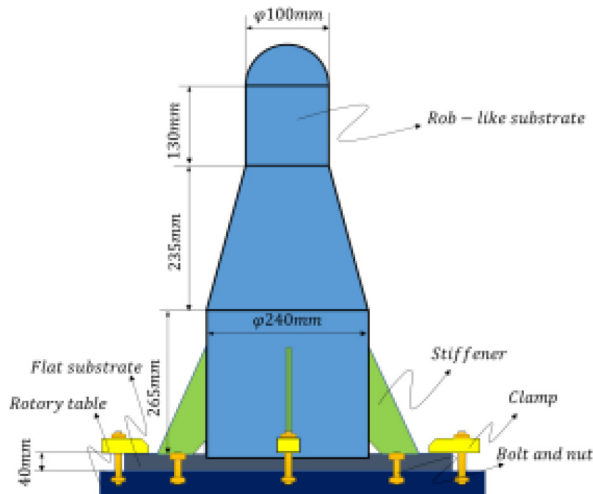
$$w = mv^{-\frac{1}{3}} + \frac{p}{r} + t$$

**Figure 21** The prototype of an underwater thruster (left), and inner blades and spindle (right)



Fit the data in Table 1 with this CSW model, and we get the regression fitting surface of the bead width as the function of the curvature radius and welding travel speed, shown in Figure 17. The specific function is  $w = 84.65v^{-\frac{1}{3}} + \frac{52.74}{r} - 1.862$ , the confidence coefficient is 98.02%, and the RMSE (root mean squared error) is 0.2777 mm.

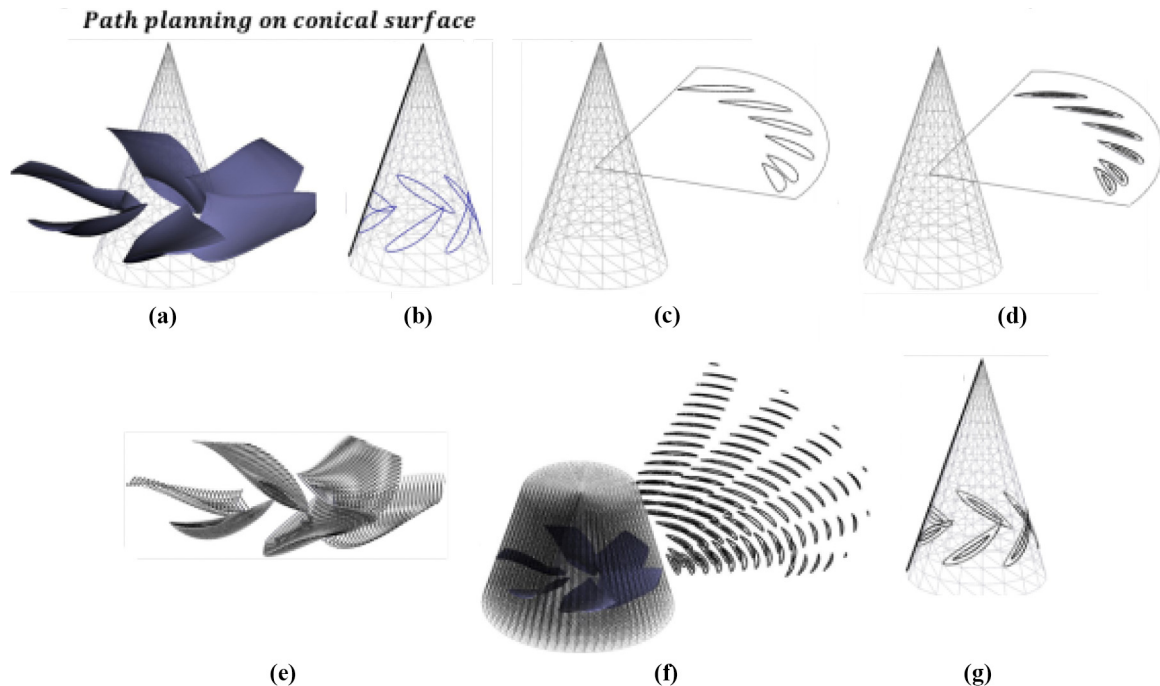
Figure 22 The substrate and its fixture



The CSW model is applied to the welding on a conical surface. The experimental setup, shown in Figure 18, consists of a three-axis CNC machine (the manufacturing accuracy is 0.01 mm), a Lorch welding machine, a two-axis rotary table. The wire material used in the experiments was stainless steel with a diameter of 1.2 mm. The shielding gas was Ar at a flow rate of 18 L/min. The rod-like substrate had the same material as the wire, and its surface consists conical and cylindrical surfaces. It was fastened onto the rotary table with four stiffeners and eight bolts to avoid looseness. In addition, a thermal infrared imager is used to monitor the temperature during the whole process. The temperature of the base part influences the flowability of the welding pool. We seek to reduce the influence by welding at a low temperature.

The tool-paths on a conical surface are shown in Figure 19, and the beads were printed from the inner path to the outer contour. As shown in Figure 20, the beads on the contours were in clockwise direction. Figure 20(a, b) shows the beads of the first layer. Figure 20(a) used a constant travel speed. The width of the outer bead changes significantly, especially at the corners. Figure 20(b) used the CSW model. The appearance at the corners gets better. Figure 20(c, d) shows the beads of the second layer, using the CSW model. However, in Figure 20(c) the weld bead of the contour flows severely. The cause could be the arc deflection, which has been explained above. To change the

Figure 23 Path planning on conical surfaces



**Notes:** (a) Constructing the parametric equation of the conical surface; (b) generating contours by slicing; (c) flattening contours onto a plane; (d) paths filling on the plane; (e) mapping paths back to the conical surface; (f) generating paths on a set of conical surfaces; (g) getting all the tool-paths



direction of the magnetic flow, we can deflect the orientations on contour by an angle  $\lambda$  around the tangent vector, shown in Figure 20(d).

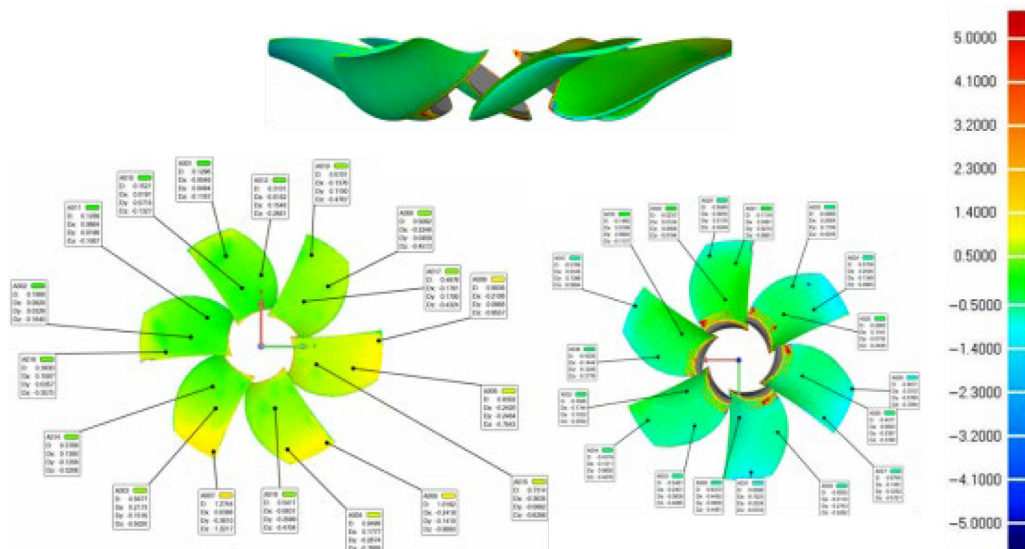
## 5. Practical fabrication

Our process planning method for both additive and five-axis processing modules are applied for the fabrication of the prototype of an underwater thruster. The underwater thruster is with large volume and heavy weight. Figure 21 shows the CAD models of this thruster and the dimension of the inner blades and spindle. The largest diameter of the thruster is about 500 mm and the height is about 400 mm, and the diameters of the largest circumcircles of the three groups of blades are 384.3 mm, 399.9 mm and 466.5 mm, respectively, from top to bottom. This component was fabricated separately, with its shell manufactured on a plane substrate by conventional 2D

Figure 24 The final WAAM part (left) and its finished part (right)



Figure 26 The deviations at selected points



slicing, and with its blades manufactured on the rod-like substrate by our surface slicing and five-axis algorithm. The top of the rod-like substrate has the same dimension with the spindle of the blades, and its bottom is welded on the flat substrate (Figure 22). To enhance the connection, another four stiffeners were welded between the bottom and the flat substrate. The flat substrate was fixed on the rotary table with bolts and nuts through the four through-holes of the flat substrate, and four clamps on the rim.

Our path planning method was used to generate the tool-paths of the blades, shown in Figure 23, including the following steps:

- Knowing the radius ( $R = 60$ ) and the height ( $H = 200$ ) of the original conical surface, it was expressed with a parametric equation  $x^2 + y^2 = 3600 \times (\frac{z}{200} - 1)^2$ ;
- Contours were generated by slicing the blades with the original conical surface;
- Using the mapping function, the contours were flattened onto a plane (note that the contour closest to the cutting line had been rotated by a certain angle to avoid being broken up);
- The contours were filled with equidistant paths on a plane;
- The tool-paths were generated by mapping the filling paths back to the conical surface;

Figure 25 The scanning of the blades





- A set of equidistant conical surfaces, in which the radius and height of the  $i_{th}$  surface were  $R_i = 60 + \frac{\sqrt{109}}{10}d \times i$ ,  $H_i = 200 + \frac{\sqrt{109}}{3}d \times i$ , were generated and used to carry out (b) (c) (d) and (e);
- Finally, we got all the tool-paths.

The blades of the underwater thruster (Figure 21) were fabricated by manufacturing a blank in our method and post-processing in CNC milling. To have the final milled part entirely covered by (or inside the body of) the blank, it was given a dimensional margin of 5.0 millimeters. The printing of a large part would be confronted with the problem of heat accumulation, leading to severe shape deformation. Thus, a homogeneous printing order was taken for each group of blades (there are three groups of blades). Taking blades in the middle group (blades with distorted surfaces) as an example, tool-paths on the same layer of the six blades were printed in sequence around the axis. If there were more than one tool-paths on a certain layer of a blade, the most inner paths of the six blades were to be printed in the first round, then the outer paths. The wire-feeding speed is 670 mm/min. The deflecting angle  $\gamma$  was set to be zero so that only four axes (including one rotating axis) were used to realize the five-axis transformation on conical or cylindrical surfaces. This was better for the rotary table with a large-weight load, and the movements were more stable. However, the weld beadings were not avoided. The CSW model was used to set the travel speed, which was ranging from 410 mm/min to 830 mm/min. The conical-surface-based blades of the final WAAM part have the largest thickness of about 40 mm on the bottom layer and about 20 mm on the top layer.

All blades had been near-net printed (Figure 24 left), which were milled to the designed dimensions (Figure 24 right). The milling process shared the same manufacturing coordinate as that of its AM process (the origin of the coordinate was the center of the flat substrate, and the z-axis was the same as the CNC system). The milling tool-paths were generated via HYPERMILL 2016.2 (the CAD/CAM software developed by OPEN MIND), and the CNC milling was carried out on SINUMERIK 840 D SL (the numerical control system developed by SIMENS). The blades had such thin thickness (the thickness of the rims was less than 1 mm) that they were very likely to deform resulting from machining force, and residual stress after machining. It should be noted that the tool-paths (both printing and milling) for the CNC system are composed of linear motion segments. To avoid the velocity and acceleration discontinuities occurring at the junction points of consecutive segments, the NC (numerical control) instruction "COMPCAD" was used to compress the consecutive segments into splines.

To learn the specific deformations of these machined blades, the points cloud of the surfaces was acquired by scanning the part via FreeScan X3. The points cloud and the original 3D model of the part were input to Geomagic Control (the reverse engineering software developed by 3D Systems) to do the best fitting and calculate the 3D deviation of the points cloud relative to the original 3D model (Figure 25). We select three points on each side of the six blades and give the specific deviations at these points (Figure 26). It is interesting that the deviations of

the points from A001 to A019 (A018 is not in the picture) are positive and the deviations from A020 to A037 are negative. The largest positive deviation is A007, which is 1.2744 mm, and the average positive deviation of these 36 points is 0.5546 mm. The largest negative deviation is A031, which is  $-0.8588$  mm, and the average negative deviation is  $-0.4718$  mm. Moreover, the closer the point is to the thin rim of the blade, the larger the deviation is. The cause could be the uneven distribution of the residual stress which forces the blades to deform (residual deformation). The finding could inspire combining subtractive processes: milling + aging treatment + milling. To be specific for the blades, the processes could be milling to a 2 mm allowance, aging treatment to release the residual stress, and milling to the required allowance. To deeply learn the relationships between the path planning strategy, the welding process, the residual stress, and the deformation, numerical simulations and more experiments are to be carried out in our future works.

## 6. Conclusion

To fabricate large metal components with overhangs built on cylindrical or conical surfaces, this study proposed an integrated slicing, tool-path planning and welding process planning method for both additive and five-axis processing modules in AM.

Both cylindrical and conical surfaces were represented with one parametric equation, which made it easy to calculate the equidistant surfaces and the intersecting contours with the overhangs. The mapping functions were constructed to flatten the contours onto planes and map the filling paths generated on planes to the surfaces. The five-axis algorithm was deduced to make the welding point to orientate toward the torch. The above methods were proved to be feasible in experiments and practical fabrications.

To improve the surface appearances of the welding beads on curved surfaces, the adaptive CSW model is investigated. The model has a confidence coefficient of 98.02%, and the RMSE of 0.2777 mm. The findings of the relationships among the curvature, travel speed and bead width on a planner plate were proved to be usable on a curved surface and used to set the travel speeds for practical fabrications. The practical fabrication of the prototype of an underwater thruster, which is hard to be fabricated in a planar AM method, shows that overhangs built on cylindrical or conical surfaces can be well fabricated in our process planning method. The reverse measuring of the blades shows the residual deformation after post-processing: an average positive deformation of about 0.5546 mm on one side and an average negative deformation of about  $-0.4718$  mm on the other side.

## References

- Bertoldi, M., Yardimci, A., Pistor, C.M. and Gucer, S.I. (1998), "Domain decomposition and space filling curves in toolpath planning and generation", *Proceedings of the 1998 Solid Freeform Fabrication Symposium*, pp. 267–274.

- Chen, L. and Tang, K. (2019), "Variable-depth curved layer fused deposition modeling of thin-shells", *Robotics and Computer-Integrated Manufacturing*, Vol. 57, pp. 422-434.
- Dai, C., Wang, C.C.L., Wu, C., Lefebvre, S., Fang, G. and Liu, Y.J. (2018), "Support-free volume printing by multi-axis motion", *ACM Transactions on Graphics*, Vol. 37 No. 4, p. 134.
- Derekar, K.S. (2018), "A review of wire arc additive manufacturing and advances in wire arc additive manufacturing of aluminium", *Materials Science and Technology*, Vol. 34 No. 8, pp. 895-916.
- Ding, Y., Akbari, M. and Kovacevic, R. (2018), "Process planning for laser wire-feed metal additive manufacturing system", *The International Journal of Advanced Manufacturing Technology*, Vol. 95 Nos 1/4, pp. 355-365.
- Ding, Y., Dwivedi, R. and Kovacevic, R. (2017), "Process planning for 8-axis robotized laser-based direct metal deposition system: a case on building revolved part", *Robotics and Computer-Integrated Manufacturing*, Vol. 44, pp. 67-76.
- Ding, D., Pan, Z., Cuiuri, D., Li, H., van Duin, S. and Larkin, N. (2016), "Bead modelling and implementation of adaptive MAT path in wire and arc additive manufacturing", *Robotics and Computer-Integrated Manufacturing*, Vol. 39, pp. 32-42.
- Dunlavey, M.R. (1983), "Efficient polygon-filling algorithms for raster displays", *ACM Transactions on Graphics (Tog)*, Vol. 2 No. 4, pp. 264-273.
- Farouki, R.T., Koenig, T., Tarabanis, K.A., Korein, J.U. and Batchelder, J.S. (1995), "Path planning with offset curves for layered fabrication processes", *Journal of Manufacturing Systems*, Vol. 14 No. 5, pp. 355-368.
- Kabakabala, D., Swathi, R., Ruan, J., Liu, X.F. and Liou, F. (2010), "A multi-axis slicing method for direct laser deposition process", *ASME International Design Engineering Technical Conferences & Computers & Information in Engineering Conference*, pp. 425-432.
- Li, H., Dong, Z. and Vickers, G.W. (1994), "Optimal toolpath pattern identification for single island, sculptured part rough machining using fuzzy pattern analysis", *Computer-Aided Design*, Vol. 26 No. 11, pp. 787-795.
- Lockett, H., Ding, J., Williams, S. and Martina, F. (2017), "Design for wire + arc additive manufacture: design rules and build orientation selection", *Journal of Engineering Design*, Vol. 28 Nos 7/9, pp. 568-598.
- Park, S.C. and Choi, B.K. (2000), "Tool-path planning for direction-parallel area milling", *Computer-Aided Design*, Vol. 32 No. 1, pp. 17-25.
- Rajan, V.T., Srinivasan, V. and Tarabanis, K.A. (2001), "The optimal zigzag direction for filling a two-dimensional region", *Rapid Prototyping Journal*, Vol. 7 No. 5, pp. 231-241.
- Ren, L., Sparks, T., Ruan, J. and Liou, F. (2008), "Process planning strategies for solid freeform fabrication of metal parts", *Journal of Manufacturing Systems*, Vol. 27 No. 4, pp. 158-165.
- Ruan, J.Z., Sparks, T., Panackal, A., Liou, F.W., Eiamsa-Ard, K., Slattery, K., Chou, H.N. and Kinsella, M. (2007), "Automated slicing for a multiaxis metal deposition system", *Journal of Manufacturing Science and Engineering*, Vol. 129 No. 2, pp. 303-310.
- Singh, P. and Dutta, D. (2001), "Multi-direction slicing for layered manufacturing", *Journal of Computing and Information Science in Engineering*, Vol. 1 No. 2, pp. 129-142.
- Sundaram, R. and Choi, J. (2004), "A slicing procedure for 5-axis laser aided DMD process", *Journal of Manufacturing Science and Engineering*, Vol. 126 No. 3, pp. 632-636.
- Wang, H., Jang, P. and Stori, J. (2001), "A metric-based approach to 2D tool path optimization for high speed machining", *American Society of Mechanical Engineers, Manufacturing Engineering Division, MED*, Vol. 13, doi: [10.1115/IMECE2002-33610](https://doi.org/10.1115/IMECE2002-33610).
- Wang, Z., Min, J. and Xiong, G. (2015), "Robotics-driven printing of curved 3D structures for manufacturing cardiac therapeutic devices", *2015 IEEE International Conference on Robotics and Biomimetics (ROBIO)*, IEEE, doi: [10.1109/ROBIO.2015.7419120](https://doi.org/10.1109/ROBIO.2015.7419120).
- Williams, S.W., Martina, F., Addison, A.C., Ding, J., Pardal, G. and Colegrove, P. (2016), "Wire + arc additive manufacturing", *Materials Science and Technology*, Vol. 32 No. 7, pp. 641-647.
- Xie, Y., Zhang, H. and Zhou, F. (2015), "Improvement in geometrical accuracy and mechanical property for arc-based additive manufacturing using metamorphic rolling mechanism", *Journal of Manufacturing Science and Engineering*, Vol. 138 No. 11.
- Xiong, J., Li, Y., Li, R. and Yin, Z. (2018), "Influences of process parameters on surface roughness of multi-layer single-pass thin-walled parts in GMAW-based additive manufacturing", *Journal of Materials Processing Technology*, Vol. 252, pp. 128-136.
- Xiong, J., Lei, Y., Chen, H. and Zhang, G. (2017), "Fabrication of inclined thin-walled parts in multi-layer single-pass GMAW-based additive manufacturing with flat position deposition", *Journal of Materials Processing Technology*, Vol. 240, pp. 397-403.
- Xu, K., Li, Y., Chen, L. and Tang, K. (2019), "Curved layer based process planning for multi-axis volume printing of freeform parts", *Computer-Aided Design*, Vol. 114, p. 114.
- Yang, J., Bin, H., Zhang, X. and Liu, Z. (2003), "Fractal scanning path generation and control system for selective laser sintering (SLS)", *International Journal of Machine Tools and Manufacture*, Vol. 43 No. 3, pp. 293-300.
- Yang, Y., Loh, H.T., Fuh, J.Y.H. and Wang, Y.G. (2002), "Equidistant path generation for improving scanning efficiency in layered manufacturing", *Rapid Prototyping Journal*, Vol. 8 No. 1, pp. 30-37.
- Yanjiang, J.X. and Ziqiu, Y. (2019), "Molten pool stability of thin-wall parts in robotic GMA-based additive manufacturing with various position depositions", *Robotics and Computer-Integrated Manufacturing*, Vol. 56, pp. 1-11.
- Youheng, F., Guilan, W., Haiou, Z. and Liye, L. (2017), "Optimization of surface appearance for wire and arc additive manufacturing of bainite steel", *The International Journal of Advanced Manufacturing Technology*, Vol. 91 Nos 1/4, pp. 301-313.

- Zhang, J. and Liou, F. (2004), “Adaptive slicing for a multi-axis laser aided manufacturing process”, *Journal of Mechanical Design*, Vol. 126 No. 2, pp. 254-261.
- Zhou, X., Zhang, H., Wang, G., Bai, X., Fu, Y. and Zhao, J. (2016), “Simulation of microstructure evolution during hybrid deposition and micro-rolling process”, *Journal of Materials Science*, Vol. 51 No. 14, pp. 6735-6749.

### **Further reading**

- Xiong, J., Yin, Z. and Zhang, W. (2016), “Closed-loop control of variable layer width for thin-walled parts in wire and arc additive manufacturing”, *Journal of Materials Processing Technology*, Vol. 233, pp. 100-106.

### **Corresponding author**

Haiou Zhang can be contacted at: [zholab@hust.edu.cn](mailto:zholab@hust.edu.cn)